

# Real-time visualisation and optimisation of acoustic waves carrying orbital angular momentum

Po-Cheng Lin , Graham M Gibson  and Miles J Padgett\* 

School of Physics and Astronomy, University of Glasgow, Glasgow G12 8QQ, United Kingdom

E-mail: [miles.padgett@glasgow.ac.uk](mailto:miles.padgett@glasgow.ac.uk)

Received 3 February 2022, revised 25 April 2022

Accepted for publication 19 May 2022

Published 8 June 2022



CrossMark

## Abstract

Travelling waves, such as light and sound, can carry angular momentum. Orbital angular momentum (OAM) is one of the components which is determined by the helicity of the phase fronts. The helical waveform is characterised in terms of an integer  $l$  and an azimuthal phase term of  $\exp(-il\theta)$ , but for  $|l| > 1$  the resulting high-order beam structure is unstable to perturbation. In this work, using Fourier transform profilometry and stroboscopic imaging techniques, we demonstrate the real-time visualisation of the OAM-carrying acoustic waveform by imaging the pressure imprint of the acoustic wave on a thin rubber sheet. Furthermore, based on the visualised waveform, we are able to optimise high-order ( $|l| > 1$ ) OAM states by controlling the individual elements of the acoustic source. Beyond the study of acoustic OAM, the real-time monitoring and optimising methods could be a benefit to other applications requiring acoustic waveform shaping, such as acoustic communications, acoustic holograms, etc.

Keywords: orbital angular momentum, acoustic wave, feedback optimisation, waveform visualisation, acoustic vortex, vortex splitting

 Supplementary material for this article is available [online](#)

(Some figures may appear in colour only in the online journal)

\* Author to whom any correspondence should be addressed.



Original content from this work may be used under the terms of the [Creative Commons Attribution 4.0 licence](#). Any further distribution of this work must maintain attribution to the author(s) and the title of the work, journal citation and DOI.

## 1. Introduction

Traveling waves transport not only energy but also linear momentum in the propagation direction. The first notion that light carries a linear momentum can be traced back to Kepler in the 1600s [1], who conjectured that the optical radiation pressure of sunlight caused the tail of a comet to always point away from the Sun. We now know that the corresponding force is proportional to the power transmitted by the light beam divided by the phase velocity of the light [2, 3]. This momentum–energy relation not only applies to transverse electromagnetic waves, such as light, but also other traveling waves such as longitudinal sound waves [3, 4]. It means for the same transmitted wave power, sound typically exerts a force a million times larger than the force from the light beam due to the comparatively slower speed of sound. For example, a typical optical tweezers can only trap micrometer-sized objects whereas acoustic tweezers can manipulate millimeter-sized objects [5].

In addition to the linear momentum, waves can also carry angular momentum. For transverse waves, such as electromagnetic waves, there are two components of angular momentum: spin angular momentum (SAM) and orbital angular momentum (OAM). The SAM is associated with the circular polarisation of the wave, which was first described by Poynting using a mechanical analogy to a revolving cylinder [6] and experimentally demonstrated by Beth [7]. As for the OAM, Allen *et al* showed that it arises from a helical phase cross-section of the beam [8]. In the case of longitudinal waves such as sound, there is no transverse polarisation and hence no SAM (inhomogeneous waves could exhibit elliptical polarisation [9]), but longitudinal waves can still carry OAM by a suitably phase-structured beam. Helically-phased waves, with the azimuthal phase in the  $xy$  plane described by  $\exp(-il\theta)$ , carry OAM with the OAM–power ratio proportional to  $l/\omega$  [4, 10–12], where  $l$  is an integer,  $\theta$  is the azimuth angle within the beam, and  $\omega$  is the frequency of the wave. Note that the centre of this helically-phased wave is a phase singularity, the rotational symmetry of which dictates that there is always destructive interference at the centre, forming a null intensity [13]. The azimuthal component of the linear momentum around the singularity gives rise to the description of the feature as an optical or acoustic vortex in the case of light or sound beams respectively [14, 15]. It should be clarified that although the existence of helically-phased fields and their associated phase singularities had been recognised since the 1970s [13], their relation to OAM was not articulated until the 1990s in the above cited work of Allen *et al* [8].

Over the years, several OAM generation methods have been proposed [16, 17]. For optical OAM, it can be generated by transmitting a plane-waved beam through a spiral phase plate or a spatial light modulator encoded with a computer-generated fork-like hologram. It is also possible to generate OAM from circularly polarised light using spin–orbit coupling devices, which can either be liquid-crystal based or based on some metamaterials [17, 18]. As for acoustic OAM, the generation of helically-phased waves is simple. Acoustic angular momentum can be produced using a circular array of speakers, each driven at the same frequency but with a phase delay given by  $l$  and their azimuth angle within the beam [10–12, 19]. Instead of controlling phases of individual speakers, the speakers themselves can be helically-shaped. Ealo *et al* [20] built a helical-shaped ultrasound transducer by gluing ferroelectret films onto a helical substrate. There are other methods based on converting planar waveforms into the helically-phased waveform, such as using the acoustic metasurface [21, 22], a Fresnel-spiral diffraction grating [23–26], or a special acoustic resonator [27].

That high-order phase singularities with  $|l| > 1$  could also exist was found very early by Nye and Berry [13]. There are now several applications that rely on the quality of high-order OAM beams and their resulting perfect null intensity region, including applications using the

multiplexing OAM for communications [28–30] and vortex coronagraphy [31]. However, such high-order states are inherently unstable under realistic conditions [13, 32]. In many experimental observations, due to any uncontrolled breaking of the symmetry, such as the existence of a coherent background or the superposition of different OAM modes, high-order vortices tend to split into sets of  $\pm 1$  vortices depending on the sign of  $l$  [33–35]. It is one objective of this current work to optimise the generation of acoustic OAM to avoid this splitting.

Since the first demonstration of OAM and vortices, several fundamental features, like amplitude and phase distributions [19], OAM transfer to matter [10, 11, 36–40], and the rotational Doppler effect [11, 41–45], have been well studied in both optical and acoustic regimes. However, the instantaneous waveform for directly showing the helical structure of the beam hasn't been demonstrated due to the difficulties in recording the large-area fast-oscillating waveform. Conventional large-array sensors, such as complementary metal-oxide-semiconductor (CMOS) cameras having frame rates around hundreds of frames per second, can only measure the slowly varying light intensity field, which is not the instantaneous phase of the waves. As for sound wave detection, it is difficult to find a microphone array with a sufficient spatial resolution for recording the spatiotemporal waveform.

In order to tackle these limitations, we visualise the acoustic waveform based on the interaction of the acoustic field with a thin rubber sheet which we view using a three-dimensional (3D) imaging technique, Fourier transform profilometry (FTP) [46, 47], and the stroboscopic imaging method [48]. We demonstrate the helical waveform of OAM beams and the suppression of the vortex splitting phenomenon in high-order OAM states by optimising individual acoustic elements based on the visualised waveform. Note that our apparatus only includes mainly low-cost 3D-printed components, common electronics, and a consumer camera, suggesting that our experiment is also a possible teaching setup for demonstrating the acoustic OAM in the classroom or to a broader audience.

## 2. Results

Our experimental setup, as shown in figure 1, consists of four parts: (i) a circular array of eight speakers with a funnel-shaped acoustic concentrator, (ii) a rubber sheet, (iii) a fringe illumination system, (iv) and a digital camera. The acoustic OAM generator is the same as that in [40] and is created using the circular array of speakers with programmed phase delays controlled by an Arduino microcontroller. The beam is focused using the acoustic concentrator and directed toward a thin silicon rubber sheet (0.1 mm in thickness). The rubber sheet is attached to a plastic ring and held by a rubber band for adjusting the evenness of the sheet tension. Through the wave–matter interaction, the pressure field of the sound beam causes the deformation of the sheet, i.e. the pressure field is encoded in the 3D height profile of the sheet. By obliquely projecting a sinusoidal fringe pattern on the surface of the sheet, the 3D height profile of the sheet can be recovered by comparing the phase difference between the original sinusoidal fringes and the deformed fringe patterns [46, 47]. Since the frequency of the sound wave (hundreds of Hertz) is higher than the frame rate of most consumer cameras (60 Hz), we use a stroboscopic illumination [48] to effectively slow down the vibration of the rubber sheet as viewed from the camera. In this case, the modulation frequency of the illuminating light is chosen to be close, but not identical, to that of the vibration. The details of the experimental setup and imaging methods can be found in the appendix section.

Figure 2 shows the temporal evolution of the reconstructed 3D height profile  $h(x, y)$  of the vibrating sheet at  $t = 0, 0.1, \text{ and } 0.2$  s, corresponding instantaneous oscillation phase  $\phi$ , and the temporally averaged amplitude  $A$  maps. The plots in the same column are for the same target OAM mode. All plots share the same  $xy$  axes as the first plot in the upper

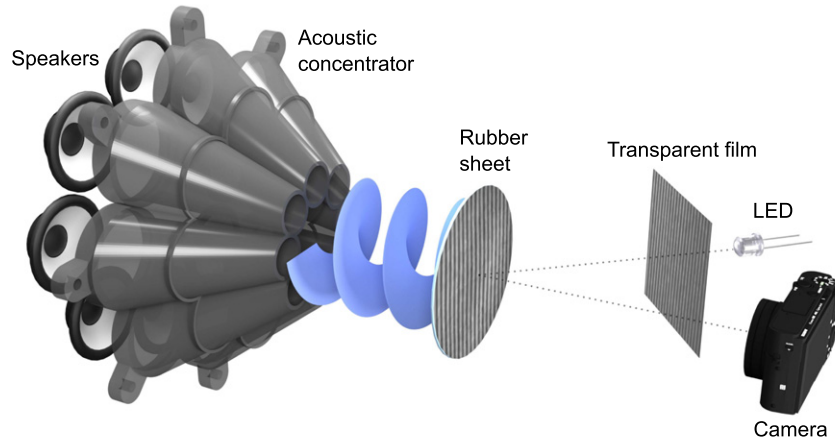


**Figure 1.** Sketch of the acoustic OAM generation system and the imaging system. The speakers generate sound waves with the same frequency (650 Hz) but with different initial phases, forming the acoustic wave with the helical wavefront. The beam is focused by the acoustic concentrator and directed to the surface of the rubber sheet. The illuminated fringe pattern on the sheet comes from the LED light, shining through a transparent film printed with a sinusoidal fringe pattern. The deformed fringe pattern with the 3D information of the sheet is recorded by a camera for further 3D height reconstruction. To record fast oscillating patterns, the LED light is modulated at a frequency close to that of the acoustic wave for effectively slowing down the patterns viewed from the camera.

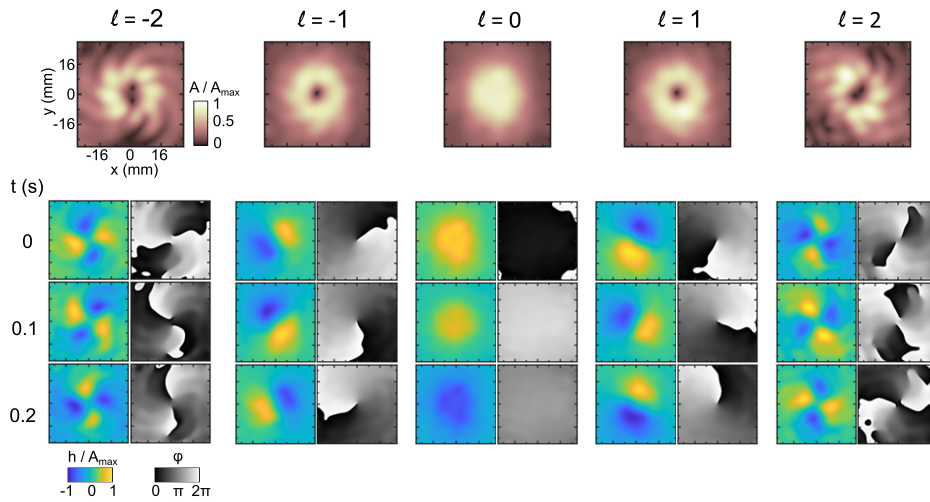


**Figure 2.** Averaged amplitude maps  $A$  (first row) and the temporal evolution of the reconstructed 3D heights  $h(x, y)$  with the corresponding oscillation phase  $\phi$  (second row) under different applied acoustic OAM fields from  $l = -2$  to 2. Plots in the same column belong to the same acoustic OAM state. The  $xy$  axes of all the plots are the same as the one at the upper left corner. The color axes are normalised according to  $A_{\max}$  of each state, where  $A_{\max} = 6, 16, 40, 16$  and  $6 \mu\text{m}$  for  $l = -2, -1, 0, 1,$  and  $2$ , respectively.

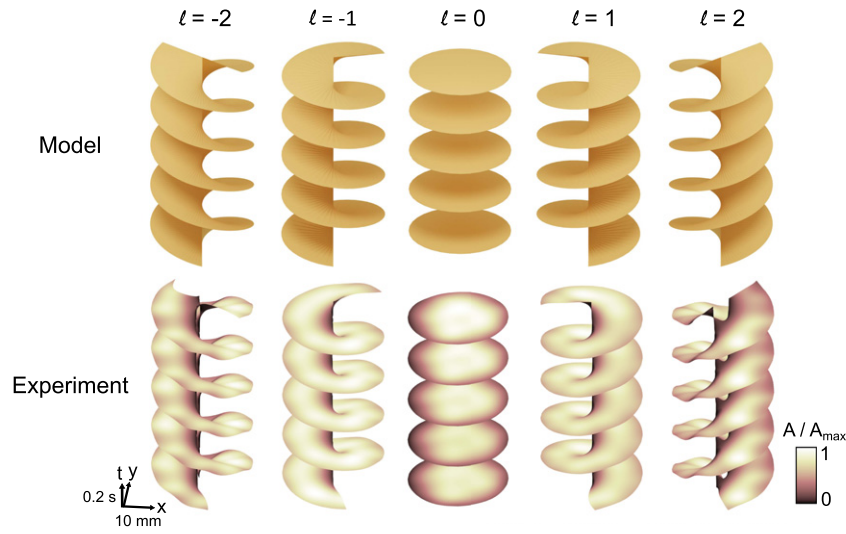


**Figure 3.** Volumetric wave crest surfaces of different acoustic OAM states. The helical waveform is the isophase ( $\phi = 0$ ) surface of  $h(x, y, t)$  in the  $xyt$  space. Note that, the actual period of the helical waveform is 1.53 ms ( $1/650$  s) instead of 0.2 s since the waveform is measured using the stroboscopic imaging. It shows good agreements between the model one and the experimental one except for the high-order OAM states with  $l = \pm 2$  due to the vortex splitting effect and the limited number of speaker sources for OAM generation.

left corner of the figure. The color axes for different OAM states follow the same normalisation as those in the  $l = -2$  state but with different  $A_{\max}$ .  $A_{\max}$  is the maximum amplitude of each state, where  $A_{\max} = 6, 16, 40, 16$  and  $6 \mu\text{m}$  for  $l = -2, -1, 0, 1$  and  $2$ , respectively.  $h(x, y, t) = A(x, y, t) \exp(i(\omega t + \phi(x, y)))$  is the surface height oscillation obtained by temporal band-pass filtering of the fundamental band (1–4 Hz) of the oscillation using inverse Fourier transform. For all the cases, the speaker concentrator to sheet distance  $d_0$  is adjusted to 6 mm in order to have uniform amplitude distribution around the centre for the  $l = 0$  plane wave state. The video showing the real-time evolution of the reconstructed waveform driven by different acoustic OAM target modes can be found in the supplementary data (<https://stacks.iop.org/JPA/55/264007/mmedia>).

From the snapshots of 3D deformations and the instantaneous phase maps, we can see the rotation of the wave crest (interface line between white and black regions) around the null intensity core. The rotation direction is either clockwise or anti-clockwise, depending upon the handedness of acoustic OAM states  $l$  ( $l > 0$  for anti-clockwise and  $l < 0$  clockwise). The averaged amplitude maps show the characteristic ‘doughnut’ shape distribution for  $l = \pm 1$  states and the Gaussian distribution for the  $l = 0$  state.

For high-order states such as  $l = \pm 2$ , instead of forming one vortex core with the topological charge  $l = \pm 2$ , there are two  $|l| = 1$  vortices with their sign depending on the topological charge  $l$  of the original states. Since we only use eight speakers to create high-order acoustic OAM, it is more likely to have the symmetry-breaking process due to the unbalanced speaker outputs or the emergence of additional OAM modes [49], which induces the vortex splitting. From figure 2, we also can see the discrete patches on amplitude maps and unstable phases at regions away from the beam centre for the  $l = \pm 2$  states.

Beyond showing 2D phase cross-sections, with the real-time measurement of the waveform  $h(x, y, t)$ , it is possible to reconstruct the volumetric wave crest structure of the OAM-carrying

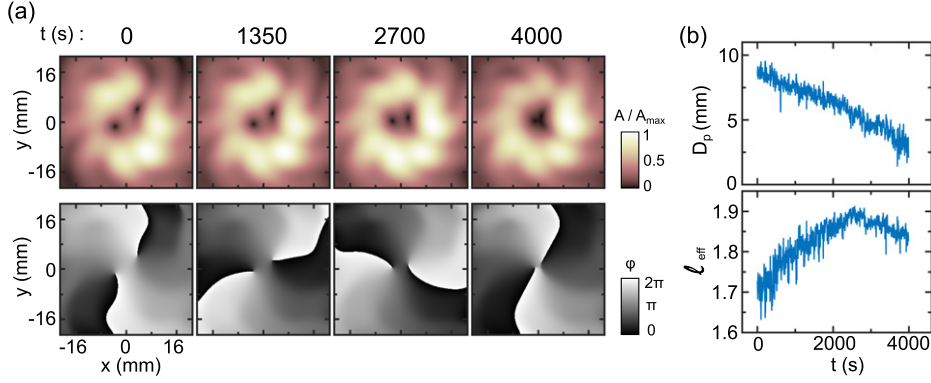


**Figure 4.** Real-time optimisation of the high-order acoustic OAM with  $l = 2$ . (a) Amplitude and phase maps of  $h(x, y, t)$  at  $t = 0, 1350, 2700$  and  $4000$  s. (b) Temporal evolution of the vortex pair distance  $D_p$  and effective topological charge  $l_{\text{eff}}$ . Instead of forming one vortex with the topological charge  $l = 2$ , there are two  $l = 1$  vortices at  $t = 0$  because of the vortex-splitting phenomenon. To suppress the effect, the individual speaker volumes are tuned automatically for minimising  $D_p$ . As time evolves,  $D_p$  and  $|l - l_{\text{eff}}|$  decrease suggesting the beam is closer to the ideal one after the optimisation.

beams in the  $xyt$  space. Figure 3 shows the isophase surface ( $\phi = 0$ ) of different OAM states with the color indicating local amplitude. We can see the good agreements between the measured crest surface from  $h(x, y, t)$  and the theoretical OAM-carrying beams for  $l = -1, 0$ , and  $1$  states. For high-order states  $l = \pm 2$ , there are some small deviations from the ideal waveform. We can also see a small gap in the centre corresponding to the effect of vortex splitting.

In response to noting that the waveform of high-order states is not perfect, with the  $xy$  position of vortices and  $h(x, y, t)$  from the visualised waveform, we are able to actively suppress the effect of vortex splitting by optimising the individual speaker sound intensities. To optimise, we use the gradient descent method [50] to adjust the amplitude of eight speakers for minimising vortex separation  $D_p$ . The problem is equivalent to finding the minimum of  $D_p$ , which is a function of the eight speaker volume  $V_i$  with  $i = 1$  to  $8$ . To have a precise measurement of  $D_p$ , we use a window with a duration equal to 6 s for each spatiotemporal phase calculation and perform the ensemble average of  $D_p$  before any changes on  $V_i$ . For every 24 s (four windows), we increase or decrease the volume of a certain speaker  $V_i$  and measure the vortex separation change  $\Delta D_p$  after the waveform relaxes to its steady state by skipping the first spatiotemporal phase calculation (first 6 s). The vortex separation change divided by the volume change gives  $\Delta D_p / \Delta V_i$ , which is the gradient of  $D_p$ . In the next time step,  $V_i$  is adjusted opposite to the gradient direction of  $D_p$  for lowering  $D_p$ . Figure 4(a) shows the amplitude and phase maps of  $l = 2$  states during the optimisation process. At  $t = 0$  s, there are two  $l = 1$  vortices instead of a single  $l = 2$  vortex. As time evolves,  $D_p$  gradually decreases (upper row of figure 4(b)) and the two vortices merge into one at  $t = 4000$  s. The video showing the evolution of amplitude and phase maps during the optimisation process is provided in the supplementary data.

To further show the improvement of the beam quality during the optimisation, we plot the time evolution of the effective OAM  $l_{\text{eff}}(t)$  calculated from  $h(x, y, t)$ , as shown in the bottom row of figure 4(b). In optical or acoustic waves, the OAM is  $lh$  per photon [8, 37, 51] or per phonon [4, 9]. The effective  $l$  can be estimated by integrating the OAM density  $j = r \times p$  over the beam cross-section and then divided by the total energy in the beam, where the transverse momentum density  $p$  is equal to the local phase gradient multiplied by the corresponding intensity. Since

the displacement field  $h(x, y)$  we measured is related to the pressure field of the acoustic wave, we can follow the similar steps used by Leach *et al* [51] to estimate  $l_{\text{eff}}$  of the waveform. The gradual decrease of  $|l - l_{\text{eff}}|$  and  $D_p$  indicate that the waveform is getting closer to the ideal waveform during the optimisation.

### 3. Discussion

With the 3D deformation measuring and stroboscopic imaging techniques, we demonstrate real-time visualisation and optimisation of OAM-carrying acoustic waveform using a low-cost apparatus. In our rough tests on the simple setup, it is able to measure the OAM-carrying waveform with the frequency from tens of Hz to 10 kHz for the 1 W speaker. We should point out that our visualisation and optimisation methods are not only limited to OAM-carrying acoustic waves, but any kind of acoustic waveform. By properly choosing the sheet material, the strobe frequency, the spatial frequency of the fringe pattern, the spatial resolution of the images captured by the camera, and the optimisation target function, the ability of real-time monitoring and optimising the large-area acoustic waveform could be beneficial to the waveform design in acoustic tweezers [5, 52], acoustic holograms [52, 53], acoustic metasurface [21, 27, 54], and acoustic communication by multiplexing OAM [30].

### Acknowledgments

PCL acknowledges financial support from Ministry of Science and Technology, Taiwan (109-2917-I-564-009). MJP thanks the Royal Society for financial support. We also like to acknowledge the financial support from Engineering and Physical Sciences Research Council to QuantIC (EP/M01326X/1).

### Data availability statement

The data that support the findings of this study are available online [55].

### Appendix A. Acoustic OAM generation

Following the method of Toninelli *et al* [40], the acoustic OAM is created by a circular array of eight speakers driven at a frequency of 650 Hz. The speakers are controlled using the digital outputs of an Arduino Due microcontroller. The microcontroller outputs eight channels of pulse-width modulated signal (330 kHz), which encode sinusoidal waves (650 Hz), each with a different phase delay. The phase delay at each channel is given by  $l \cdot \theta$  where  $\theta$  is the azimuthal angle of the speaker that is connected to this channel. To recover the sinusoidal wave from the pulse-width modulated signal, each output channel is connected to a low-pass Chebyshev filter for removing the high-frequency carrier wave. After filtering, the sinusoidal waves are amplified and applied to speakers for generating loud acoustic waves. To further enhance the local sound pressure, a funnel-shaped acoustic concentrator consisting of eight individual sound-guides is designed. It is made by a 3D printer using polylactic acid material. The diameter of the sound beam is reduced from 10 cm to 2 cm, which is the diameter of the small-end of the funnel. With the acoustic concentrator, the vibration of the sheet is larger and more visible for measuring.

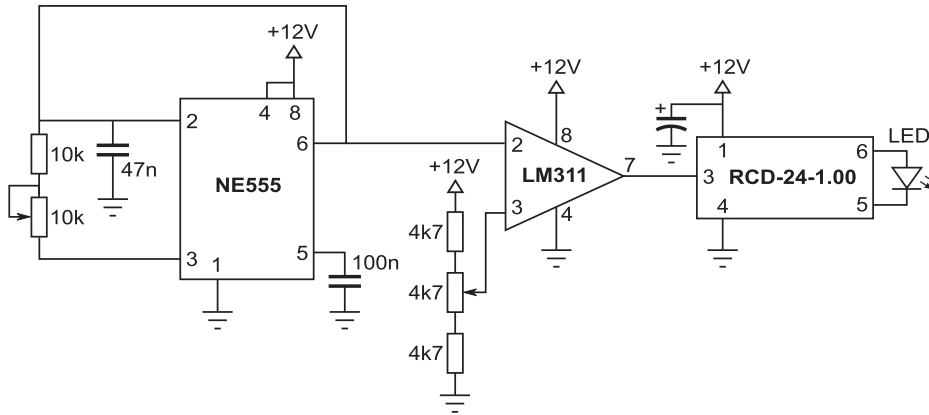


**Figure B1.** The circuit diagram of the LED driver with the variable frequency and duty cycle controls. In this circuit, the 555 timer (NE555) is used as a triangular wave generator. The triangular wave is generated at the trigger/threshold (2/6) port of the NE555 through charging and discharging at the output port (3), with the frequency determined by the RC circuit. Then, the voltage of the triangular wave is compared with a reference voltage at port 3 of the operational amplifier (LM311). The voltage divider at port 3 of the LM311 can control the duty cycle of the pulse wave at the output port (7). The pulse wave determines the frequency and duty cycle of output from the LED driver (RCD-24-1.00) which controls the power delivered to the LED for the stroboscopic illumination.

## Appendix B. Imaging system

There are two parts in the imaging system: (1) FTP for reconstructing 3D deformation of the vibrating sheet from the 2D images captured by a camera, and (2) stroboscopic illumination for effectively decreasing the frequency of repetitive patterns viewed from the camera.

FTP is a non-contact 3D profile measuring technique based on detecting the distortion of a periodic pattern due to the undulated surface [46, 47]. In our setup (see figure 1), the LED light shines through a transparent film printed with a sinusoidal fringe pattern and subsequently creates the fringe pattern on the surface of the rubber sheet. The information of 3D shape of the sheet is encoded into the deformed fringe pattern which can be captured by a camera. Based on the optical geometry of the FTP [46], it was shown that the object local deformation  $h$  is proportional to the local phase difference between the original fringe pattern and the deformed one. To get the phase of the sinusoidal fringe pattern, a 2D Fourier transform is used to filter and select the fundamental components in the spectrum. The inverse Fourier transform of the fundamental component gives the complex signal, which contains the phase information of the pattern. By applying the above processes to all the images and comparing their phase differences with the original one, the dynamics of the vibrating sheet  $h(x, y, t)$  can be reconstructed. Note that, since the phase calculation gives the values ranging from  $-\pi$  to  $\pi$ , and has discontinuities with  $2\pi$  phase jumps, a 2D phase unwrapping algorithm is applied for obtaining the continuous phase distribution [47].

Although we can use FTP to get the 3D deformation of the sheet, it is still difficult to record its dynamics driven by acoustic waves because the vibration frequency (650 Hz) is higher than the capturing framerate (30 Hz) of a conventional camera. To tackle this problem, we use stroboscopic illumination to effectively reduce the vibration frequency viewed from the camera. Stroboscopic effect can be realised by flashing the light source at a frequency close to

the frequency of the cyclic motion [48]. If the frequency of the flashes is slightly smaller, each flash can illuminate the following oscillation pattern of the sheet. Due to the aliasing effect, the effective frequency of the oscillation viewed from the camera is the frequency difference between the flashing and the oscillation.

The circuit diagram shown in figure B1 is the strobe light LED driver with the variable frequency and variable duty cycle output. The frequency of the LED pulses is adjusted to 648 Hz and 10% duty cycle for decreasing the effective vibration frequency of the sheet viewed from the camera. The circuit is composed of a triangular wave oscillator (NE555), a comparator (LM311), and a LED driver (RCD-24.1.00). By adjusting the RC charging/discharging time scale of the oscillator and the reference voltage at the comparator, the circuit can output pulse signals with different frequencies and duty cycles.

## ORCID iDs

Po-Cheng Lin  <https://orcid.org/0000-0002-1005-3507>

Graham M Gibson  <https://orcid.org/0000-0003-0051-8654>

Miles J Padgett  <https://orcid.org/0000-0001-6643-0618>

## References

- [1] Kepler J 1619 *De Cometis: Libelli Tres* (Augsburg: Typis Andre Apergeri, sumptibus Sebastiani Mylii bibliopol Augustani) <https://books.google.co.uk/books?id=5Z1BQAAACAAJ>
- [2] King L V 1934 *Proc. R. Soc. A* **147** 212–40
- [3] Peskin C S 2010 Wave momentum [https://math.nyu.edu/faculty/peskin/papers/wave\\_momentum.pdf](https://math.nyu.edu/faculty/peskin/papers/wave_momentum.pdf)
- [4] Lekner J 2006 *J. Acoust. Soc. Am.* **120** 3475–8
- [5] Ozcelik A, Rufo J, Guo F, Gu Y, Li P, Lata J and Huang T J 2018 *Nat. Methods* **15** 1021–8
- [6] Poynting J H 1909 *Proc. R. Soc. A* **82** 560–7
- [7] Beth R A 1936 *Phys. Rev.* **50** 115–25
- [8] Allen L, Beijersbergen M W, Spreeuw R J C and Woerdman J P 1992 *Phys. Rev. A* **45** 8185–9
- [9] Bliokh K Y and Nori F 2019 *Phys. Rev. B* **99** 174310
- [10] Volke-Sepúlveda K, Santillán A O and Boulosa R R 2008 *Phys. Rev. Lett.* **100** 024302
- [11] Skeldon K D, Wilson C, Edgar M and Padgett M J 2008 *New J. Phys.* **10** 013018
- [12] Demore C E M, Yang Z, Volovick A, Cochran S, MacDonald M P and Spalding G C 2012 *Phys. Rev. Lett.* **108** 194301
- [13] Nye J F and Berry M V 1974 *Proc. R. Soc. A* **336** 165–90
- [14] Couillet P, Gil L and Rocca F 1989 *Opt. Commun.* **73** 403–8
- [15] Hefner B T and Marston P L 1999 *J. Acoust. Soc. Am.* **106** 3313–6
- [16] Padgett M J 2017 *Opt. Express* **25** 11265–74
- [17] Wang X, Nie Z, Liang Y, Wang J, Li T and Jia B 2018 *Nanophotonics* **7** 153–1556
- [18] Ambrosio A 2018 *J. Opt.* **20** 113002
- [19] Thomas J-L and Marchiano R 2003 *Phys. Rev. Lett.* **91** 244302
- [20] Ealo J L, Prieto J C and Seco F 2011 *IEEE Trans. Ultrason. Ferroelectr. Freq. Control* **58** 1651–7
- [21] Esfahlani H, Lissek H and Mosig J R 2017 *Phys. Rev. B* **95** 024312
- [22] Naify C J, Rohde C A, Martin T P, Nicholas M, Guild M D and Orris G J 2016 *Appl. Phys. Lett.* **108** 223503
- [23] Jiménez N, Picé R, Sánchez-Morcillo V, Romero-García V, García-Raffi L M and Staliunas K 2016 *Phys. Rev. E* **94** 223503
- [24] Jiménez N, Romero-García V, García-Raffi L M, Camarena F and Staliunas K 2018 *Appl. Phys. Lett.* **112** 204101
- [25] Muelas-Hurtado R D, Ealo J L, Pazos-Ospina J F and Volke-Sepúlveda K 2018 *Appl. Phys. Lett.* **112** 084101

- [26] Muelas-Hurtado R D, Ealo J L and Volke-Sepúlveda K 2020 *Appl. Phys. Lett.* **116** 114101
- [27] Jiang X, Li Y, Liang B, chun Cheng J and Zhang L 2016 *Phys. Rev. Lett.* **117** 034301
- [28] Gibson G, Courtial J, Padgett M J, Vasnetsov M, Pas'ko V, Barnett S M and Franke-Arnold S 2004 *Opt. Express* **12** 5448–56
- [29] Wang J et al 2012 *Nat. Photon.* **6** 488–96
- [30] Shi C, Dubois M, Wang Y and Zhang X 2017 *Proc. Natl Acad. Sci. USA* **114** 7250–3
- [31] Foo G, Palacios D M and Swartzlander G A 2005 *Opt. Lett.* **30** 3308–10
- [32] Freund I 1999 *Opt. Commun.* **159** 99–117
- [33] Kumar A, Vaity P and Singh R P 2011 *Opt. Express* **19** 6182
- [34] Ricci F, Löffler W and van Exter M P 2012 *Opt. Express* **20** 22961
- [35] Neo R, Tan S J, Zambrana-Puyalto X, Leon-Saval S, Bland-Hawthorn J and Molina-Terriza G 2014 *Opt. Express* **22** 9920
- [36] He H, Friese M E J, Heckenberg N R and Rubinsztein-Dunlop H 1995 *Phys. Rev. Lett.* **75** 826–9
- [37] O'Neil A T, MacVicar I, Allen L and Padgett M J 2002 *Phys. Rev. Lett.* **88** 053601
- [38] Padgett M and Bowman R 2011 *Nat. Photon.* **5** 343–8
- [39] Marzo A, Caleap M and Drinkwater B W 2018 *Phys. Rev. Lett.* **120** 044301
- [40] Toninelli E, Cox M A, Gibson G M, Brown S D, Edgar M P, Forbes A and Padgett M J 2019 *Sci. Rep.* **9** 1–9
- [41] Gibson G M, Toninelli E, Horsley S A R, Spalding G C, Hendry E, Phillips D B and Padgett M J 2018 *Proc. Natl Acad. Sci. USA* **115** 3800–3
- [42] Cromb M, Gibson G M, Toninelli E, Padgett M J, Wright E M and Faccio D 2020 *Nat. Phys.* **16** 1069–73
- [43] Li G, Zentgraf T and Zhang S 2016 *Nat. Phys.* **12** 736–40
- [44] Barreiro S, Tabosa J W, Failache H and Lezama A 2006 *Phys. Rev. Lett.* **97** 113601
- [45] Zhou H, Fu D, Dong J, Zhang P and Zhang X 2016 *Opt. Express* **24** 10050
- [46] Takeda M and Mutoh K 1983 *Appl. Opt.* **22** 3977
- [47] Su X and Chen W 2001 *Opt. Lasers Eng.* **35** 263–84
- [48] Veen F V 1977 *Handbook of Stroboscopy* (Concord, MA: General Radio)
- [49] Liu R, Phillips D B, Li F, Williams M D, Andrews D L and Padgett M J 2015 *J. Opt.* **17** 045608
- [50] Ruder S 2017 An overview of gradient descent optimization algorithms (arXiv:1609.04747)
- [51] Leach J, Yao E and Padgett M J 2004 *New J. Phys.* **6** 71
- [52] Marzo A and Drinkwater B W 2019 *Proc. Natl Acad. Sci. USA* **116** 84–9
- [53] Melde K, Mark A G, Qiu T and Fischer P 2016 *Nature* **537** 518–22
- [54] Assouar B, Liang B, Wu Y, Li Y, Cheng J-C and Jing Y 2018 *Nat. Rev. Mater.* **3** 460–72
- [55] Lin P-C, Gibson G M and Padgett M J 2022 Real-time Visualisation and Optimisation of Acoustic Waves Carrying Orbital Angular Momentum